Journal of Polymer Research (2023) 30:257
https://doi.org/10.1007/s10965-023-03639-0

ORIGINAL PAPER

Fabrication of poly(lactic acid)-cellulose acetate core-shell electrospun fibers with improved tensile strength and biocompatibility for bone tissue engineering

Muhammad Faiq Abdullah[1,2,5] · Andri Andriyana[3,5] · Farina Muhamad[4,5] · Bee Chin Ang[1,5]

Received: 5 January 2023 / Accepted: 4 June 2023 / Published online: 13 June 2023

Abstract

The employment of individual poly(lactic acid) (PLA) or cellulose acetate (CA) electrospun fibers as bone tissue replacement was restricted by the weak mechanical properties of CA and the poor cell-affinity of PLA. In this study, core-shell fibers with PLA as the core component and CA as the shell layer were fabricated via coaxial electrospinning with significant improvements in the tensile strength and biocompatibility in comparison to individual PLA and CA fibers and blend PLA/CA fibers. The employment of a core-to-shell flow rate ratio of 0.25:0.5 mL/hr:mL/hr resulted in the formation of defect-free and uniformly distributed PLA-CA core-shell fibers (cs-PLA1-CA2) with the highest ultimate tensile strength (19.53 ± 1.68 MPa) and Young's modulus (0.62 ± 0.09 GPa) among all core-shell fibers produced in this study. These tensile values match the tensile properties of native cancellous bone and represent around a 130% and 160% improvement in strength and stiffness compared to monolithic CA fibers, respectively. Higher weight fraction and improved crystallinity of PLA-core were revealed to contribute to this mechanical enhancement of cs-PLA1-CA2. An in vitro biocompatibility study was conducted using human fetal osteoblasts (hFOB). The results indicate improved cell distribution, better cell-scaffold attachment, and higher cell proliferation and alkaline phosphatase (ALP) activity of cs-PLA1-CA2 compared to monolithic PLA and blend PLA/CA fibers, while matching the growth performance of hFOB seeded on tissue culture polystyrene (TCP). The PLA-CA core-shell fibers produced in this study hold great promise for use as bone tissue scaffolds.

Keywords Core-shell fibers · Coaxial electrospinning · Poly(lactic acid) · Cellulose acetate · Tissue engineering · Scaffolds

✉ Andri Andriyana
andri.andriyana@um.edu.my

✉ Farina Muhamad
farinamuhamad@um.edu.my

✉ Bee Chin Ang
amelynang@um.edu.my

[1] Department of Chemical Engineering, Faculty of Engineering, Universiti Malaya, Kuala Lumpur 50603, Malaysia

[2] Faculty of Chemical Engineering and Technology, Universiti Malaysia Perlis, Kompleks Pusat Pengajian Jejawi 3, Arau, Perlis 02600, Malaysia

[3] Department of Mechanical Engineering, Faculty of Engineering, Universiti Malaya, Kuala Lumpur 50603, Malaysia

[4] Department of Biomedical Engineering, Faculty of Engineering, Universiti Malaya, Kuala Lumpur 50603, Malaysia

[5] Centre of Advanced Materials, Faculty of Engineering, Universiti Malaya, Kuala Lumpur 50603, Malaysia

Introduction

Bone tissue engineering emerges as the alternative to the conventional bone defect treatments with the main goal to maintain, enhance and restore bone tissue functions. Usually, this goal could be achieved by fabricating a scaffold that closely mimics native extracellular matrix (ECM) [1]. The natural ECM comprises of assorted interwoven protein fibers with size less than hundreds of nanometers [2]. Therefore, developing submicron or nano-size scaffolds that resemble the architecture and features of native ECM is the most challenging area in the tissue engineering field. The ideal bone tissue scaffolds must possess several key criteria to ensure their suitability and practicality to be employed in bone tissue engineering. These include biocompatible and non-toxic characteristics, mechanical properties which closely match to that of native bone, surface epitopes which stimulating cells adhesion and proliferation (osteoconductive), and high interconnected porosity with sufficient pore size [3].

One way to achieve all these biomaterial criteria is by fabricating fibrous scaffolds with a core–shell structure. Among various fabrication techniques developed to construct core–shell fibrous scaffolds, coaxial electrospinning has made the most progress in terms of achieving desired fiber structures, ease of physicochemical modifications, and experimental and modelling developments of the core–shell fibers [4, 5]. The establishment of core–shell fibers solves many restrictions that were associated with monolithic fibers. For instance, core–shell structure allows modification as well as enhancement of the physical and mechanical properties of the electrospun fibers [4]. Furthermore, the core–shell structure also offers a unique opportunity for cell adhesion improvement by ensuring only material with excellent cell-affinity exists on the surface of the fibrous scaffolds [6, 7].

Poly(lactic acid) (PLA) has fast emerged as one of the most promising synthetic polymers to be used for the development of tissue scaffolds, including for bone regeneration due to its inherent biodegradability, remarkable tensile properties, and good processability [3, 8]. Nevertheless, the employment of individual PLA fibers as bone tissue scaffolds was restricted by their other unfavorable properties. The biggest drawback of PLA is its hydrophobicity and lack of cell-recognition functional groups at its surface, which lead to poor cell attachment, spreading, and proliferation [9, 10]. Therefore, a new strategy is needed to overcome the limitations of PLA while maintaining its favorable properties, which is the focus of the current study.

Cellulose acetate (CA), on the other hand, is gaining ever-increasing popularity as a standout material among natural polymers to be used in biomedical applications, including tissue engineering. This is owing to its inherent biocompatibility [11, 12], biodegradability, and good electrospinnability and solubility in various solvents [13, 14]. Additionally, CA, as the most valuable cellulose derivative, is also renewable with a relatively low synthesizing cost [15], and it possesses excellent resistance to chemicals and heat [16]. All these characteristics have further elevated the status of CA as one of the preferred materials for the fabrication of tissue-engineered scaffolds. Despite possessing remarkable biocompatibility, the poor tensile properties of CA represent the primary hindrance limiting its application as a bone tissue scaffold. One of the common strategies implemented by researchers to enhance the mechanical properties of CA fibers is through physical or chemical crosslinking [17–19] and post-chemical treatment (e.g., using potassium chloride [20] or calcium hydroxide [21]). Nevertheless, several problems are still associated with these strategies, including the reported cytotoxic effects of the most common crosslinking agent, i.e., glutaraldehyde [22, 23], as well as high curing temperatures (> 100 °C) [18, 24, 25] and long curing times (> 24 h) [26, 27] when natural crosslinkers were used.

Another simple and effective approach to improving the mechanical properties of CA is by blending CA with mechanically superior polymers such as PLA [28, 29], followed by uniaxial electrospinning of the blend solution. Even this strategy has its own constraints. While the initial aim of polymeric blending is to take advantage of the desired individual properties of the material [28, 30], the undesirable properties of the other materials remain and might affect the performance of the blend fibers. For example, in a PLA/CA blend, the lack of cell recognition-sites in PLA remains on the fiber surface, which may impede the potential cell adhesion. Combining them in a unique core–shell structure might be the solution to this impasse. Core PLA was designed to provide the overall tensile strength of the core–shell fibers, while shell CA improves the interaction between the scaffold and cell. In addition, the core–shell structure offers the exciting advantage of ensuring only the desired CA is on the outer surface of the fibrous scaffolds, which may improve bone cell attachment.

While it is acknowledged that the fabrication of PLA-CA core–shell fibers has been reported by Naseri-Nosar and coworkers [31], the aforementioned fibers were fabricated using wet coaxial electrospinning (i.e., a water bath as a collector) which may add further complication for future modification of the fibers. For example, future works may involve the incorporation of osteoinductive drugs or molecules to improve the osteogenicity of the PLA-CA core–shell fibrous scaffold. Therefore, if these drugs or molecules are to be loaded in the fibers collected in a water bath, the drugs may be rapidly eluted out during the fabrication process, and sustained release of the drugs is unable to be achieved.

In this study, the PLA-CA core–shell fibers were prepared via dry coaxial electrospinning, and the effect of the core-to-shell flow rate ratio on the morphology, tensile properties, and thermal behavior of the as-produced core–shell fibers were discussed in detail. Subsequently, the in vitro biocompatibility of PLA-CA core–shell electrospun fibers was evaluated against human fetal osteoblasts (hFOB) 1.19 cell-line in comparison to monolithic PLA and CA fibers, and blend PLA/CA fibers. The cellular response was measured and compared in terms of cell proliferation, viability, alkaline phosphatase (ALP) activity, and cellular morphology. To the best of our knowledge, the application of PLA-CA core–shell fibers as potential bone tissue scaffolds is yet to be evaluated, and this represents the main motivation of this work.

Experimental section

Materials

PLA granules (trade name Ingeo 3052D, D-isomer content ~ 4%, $\rho = 1.24$ g/cm^3, $M_w = 94{,}000$–$115{,}000$ g/mol) were

purchased from NatureWorks LLC, Minnesota, USA while CA powder (acetyl group of 29–45%, $\rho = 1.28$ g/cm^3) was obtained from R&M Chemicals, Malaysia. The degree of acetyl substitution (DS) is ~ 2.7, as provided by the manufacturer. Meanwhile, 1,1,1,3,3,3-hexafluoro-propan-2-ol (HFIP) was acquired from Wuhan Huaxiang Kejie Biotechnology Corp. Ltd., China and was employed as a solvent for PLA and CA dissolution. All chemicals were of analytical grade and used as received.

Electrospinning

Prior to the formation of PLA-CA core–shell fibers, monolithic PLA and CA fibers were first fabricated using uniaxial electrospinning. 12 wt% of the PLA solution was prepared by dissolving 1.2 g PLA granules in 5.51 mL of HFIP. In a separate dissolution process, 8 wt% of CA solution was prepared by adding 0.8 g of CA powder to 5.76 mL of HFIP. Both PLA and CA dissolution were performed separately in a closed glass bottle at 25 °C with continuous stirring at 250 rpm for at least 8 h or until a clear solution was formed. The freshly prepared PLA and CA solution were then immediately spun via uniaxial electrospinning to yield monolithic PLA and CA fibers by employing these parameters; 15 kV applied voltage, 15 cm distance from needle-tip to collector, and 1 mL/hr flow rate.

PLA-CA core–shell fibrous scaffolds (denoted as cs-PLA-CA), on the other hand, were fabricated via coaxial electrospinning. The schematic diagram of the coaxial electrospinning setup for the preparation of cs-PLA-CA fibrous scaffolds is depicted in Fig. 1. The setup consisted of a high voltage supplier (PS-35PCL, Progene Link Sdn. Bhd., Malaysia), two syringe pumps (NLS20, Progene Link Sdn. Bhd., Malaysia), a stainless-steel plate collector, and a custom-built coaxial needle. The core needle size was 22G, while the shell needle size was 16G. The same PLA (12 wt%) and CA (8 wt%) solutions that were used for the formation of monolithic PLA and CA fibers were injected as core and shell working solutions, respectively, through the coaxial needle to fabricate PLA-CA core–shell fibers. Three different PLA-CA core–shell electrospun fibers were prepared by varying core-to-shell flow rate ratios of 0.5:0.5, 0.25:0.5, and 0.1:0.5 mL/hr:mL/hr. These PLA-CA core–shell electrospun fibers were designated as cs-PLA1-CA1, cs-PLA1-CA2, and cs-PLA1-CA5, respectively. All PLA-CA core–shell fibrous samples were fabricated using 12 kV applied voltage and collected on an aluminum foil-covered stainless-steel plate collector with a needle tip-to-collector distance of 15 cm. The employment of high voltage (i.e., 15 kV) resulted in unstable jet stretching and eventually jet splaying or branching, speculated to be due to excessive charge repulsion at this voltage value. Therefore, 12 kV applied voltage was employed during coaxial electrospinning as it provided adequate Coulombic repulsion force to achieve stable jet stretching.

As a comparison, blend PLA/CA electrospun fibers were also fabricated in this study. The blend PLA/CA solution was prepared at 50:50 w/w of 12 wt% PLA and 8 wt% CA solution in HFIP. For instance, 0.6 g PLA granule in 2.76 mL HFIP (which represents 5 g of 12 wt% PLA) was mixed with 0.4 g CA powder in 2.88 mL HFIP (which represents 5 g of 8 wt% CA) to yield 10 g of a blend PLA/CA 50:50 w/w solution. The freshly prepared PLA/CA solution was then spun via uniaxial electrospinning using these parameters; 1 mL/hr flow rate, 15 kV applied voltage, and 15 cm needle tip-to-collector distance. The as-produced blend PLA/CA fibers were designated as b-PLA/CA. All electrospinning experiments in this study were conducted in a fume hood at 25 °C ± 1 °C and < 75% relative humidity. The collected samples were kept in the fume hood for at least 48 h to allow complete removal of the solvent through evaporation.

Morphological and structural characterization

The morphologies of all fabricated electrospun fibers (i.e., monolithic PLA and CA, cs-PLA-CA, and b-PLA/CA) were examined by a field emission scanning electron microscope (FESEM) (Sigma 300, Zeiss, Germany) using a low accelerating voltage of 1 kV to prevent charging during image acquisition. Subsequently, fiber diameter (D_f)

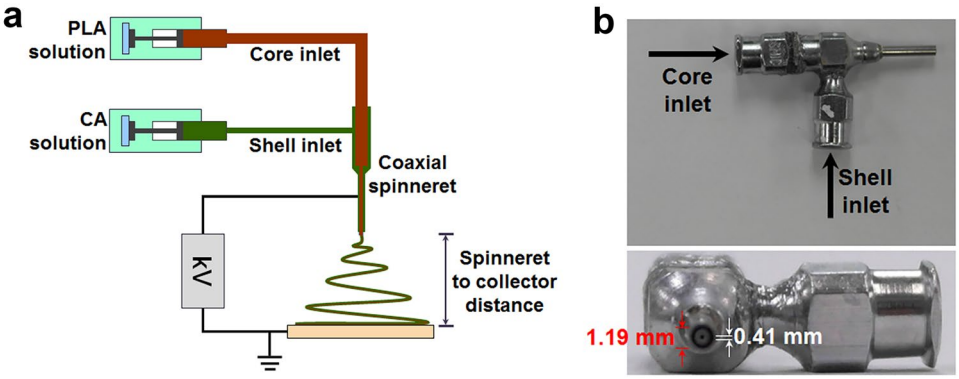

Fig. 1 **a** Schematic diagram of the coaxial electrospinning setup for the fabrication of cs-PLA-CA fibrous scaffolds. **b** Digital image of a custom-built coaxial needle

was measured by ImageJ software (National Institutes of Health, USA), and the average D_f was calculated from at least 100 fibers. In addition, the histogram of the D_f distribution was plotted using OriginPro software (version 2021, OriginLab Corporation, Northampton, Massachusetts, USA). Apart from the all-important D_f and D_f distribution, the pore size of the fibrous scaffolds was also estimated using the "Analyze Particles" built-in plugin in ImageJ software. The pore sizes were averaged and reported as mean ± standard deviation (SD).

Meanwhile, the core–shell structure of the as-produced PLA-CA core–shell fibers was confirmed by a high-resolution transmission electron microscopy (HRTEM) (Tecnai G2 20 S-Twin, FEI, Oregon, USA). The samples for TEM were prepared by directly spinning PLA-CA core–shell fibers onto a lacey carbon film copper grid (LC300-CU, 300 Mesh, Electron Microscopy Sciences, Pennsylvania, USA) for 5–7 s. The collected fibers were kept in a drying cabinet for at least 24 h to allow complete removal of the solvent prior to TEM viewing. The fibrous samples were then observed using an acceleration voltage of 150 kV.

Surface chemistry analysis

The surface chemistry of all electrospun fibrous scaffolds was analyzed by Fourier transform infrared (FTIR) spectroscopy using a single attenuated total reflectance (ATR) mode (Spectrum 2000, Perkin Elmer, Massachusetts, USA). Prior to analysis, the fibrous samples were cut into 10 mm × 10 mm squares. The specimen was then placed on the sample stage and pressed with the detector. The spectra were attained in the wavelength range of 400–4000 cm^{-1} as an average of 32 scans with 2 cm^{-1} resolution.

Tensile testing

The tensile properties of the monolithic PLA, CA, PLA-CA core–shell, and blend PLA/CA electrospun fibrous scaffolds were determined using a uniaxial tensile tester (Shimadzu AGS-X Series), following similar testing methods as in our previous study [32]. Prior to testing, the electrospun fibrous mats were cut into a 60 mm × 10 mm rectangular shape. 5 replicate specimens were prepared for each sample. Subsequently, the fiber percentage (P_f) of each specimen was calculated [32] and was used to determine the effective tensile stress of the fibrous scaffolds. The tensile testing was performed by stretching the specimen until it broke using a strain rate of 0.001/s. The gauge length was fixed at 40 mm with a 500 N load cell.

Thermal analysis

The thermal properties of all electrospun fibrous scaffolds produced in this study were determined using differential scanning calorimetry (DSC) (DSC 3, Mettler-Toledo, Switzerland). 5 – 10 mg of the fibrous samples were heated from 30 °C—300 °C at a heating rate of 5 °C/min under a nitrogen gas atmosphere. Critical thermal properties such as glass transition temperature (T_g), melting temperature (T_m), cold-crystallization temperature (T_{cc}), melt-recrystallization temperature (T_{mc}), and enthalpy changes were then determined from the DSC thermograms. Subsequently, the crystallinity percentage (X_c) of the samples was calculated using Eq. (1) [33]:

$$X_c(\%) = \frac{\Delta H_m - \Delta H_{cc,mc}}{\Delta H_m^{\circ} \times w_i} \times 100 \quad (1)$$

where ΔH_m is the melting enthalpy of the sample, $\Delta H_{cc,mc}$ is the cold crystallization and/or melt-recrystallization enthalpy of the sample, ΔH_m° is the melting enthalpy of a purely crystalline sample (i.e., 93.7 J/g for PLA [34–36] and 58.8 J/g for CA [37, 38]), and w_i is the weight fraction of PLA or CA in the sample. For comparison, PLA granules and CA powder were also subjected to similar thermal testing.

In vitro biocompatibility study

Cell culture and seeding

Human fetal osteoblasts 1.19 cell lines (hFOB 1.19) (CRL-11372™, ATCC-Biomedia, Malaysia) were used in this study. hFOB 1.19 were cultured in a complete growth medium of Dulbecco's Modified Eagle's Medium (DMEM F12, Sigma-Aldrich, Malaysia), supplemented with 10% fetal bovine serum (FBS, Gibco, USA) and 1% geneticin (G418, Thermo Fisher, Waltham, USA). The cells were cultured in an incubator (Galaxy 170 S, New Brunswick, Eppendorf AG, Germany) at 34 °C in a humidified environment (5% CO_2, 95% air). Once cells reached ~90% confluence, they were detached using Accutase® (Innovative Cell Technologies Inc., USA). Prior to cell seeding, the electrospun fibrous scaffolds were cut into 10 mm × 10 mm squares and underwent a series of pre-culture treatments, i.e., 1 h immersion in 70% ethanol, 2 times rinsing with 1X phosphate buffer saline (PBS) (Sigma Aldrich, Malaysia), and re-immersion in culture medium for another 1 h. For PLA-CA core–shell fibers, only cs-PLA1-CA2 was selected for biocompatibility study in comparison to PLA, CA, and b-PLA/CA fibers. 3×10^4 cells (20 µL, passage 5 cells) were then seeded onto each fibrous square and incubated for 2 h (34 °C,

5% CO_2). After 2 h, 1 mL of complete growth medium was added to submerge the fibrous scaffolds. The culture medium was changed every 2–3 days. At pre-determined time points, the cells cultured on different fibrous scaffolds were characterized through various assays to compare the quality of the cell growth. As a control, cells were also seeded on a tissue culture polystyrene (TCP) plate.

Cell proliferation

The cell proliferation was assessed using the AlamarBlue (AB) assay (Invitrogen, Massachusetts, USA) at four different time points, i.e., days 1, 4, 7, and 14. At a predetermined time point, the growth medium in each well containing a cell-seeded scaffold was removed and replaced by 1 mL of a 10% v/v AB solution. The samples were re-incubated for 4 h at 34 °C in a 5% CO_2 environment. Triplicates of 100 µL AB working solution were then aspirated from each well containing a cell-seeded scaffold into a new 96-well plate. The absorbance of the test sample was measured at 570 nm by a multi-mode microplate reader (FLUOstar® Omega, BMG LabTech, Germany), and 595 nm was set as the reference wavelength. The blank for each test sample was prepared by incubating the unseeded scaffolds under similar conditions in an AB solution.

Morphology of seeded cells

The morphology of the seeded cells was analyzed by scanning electron microscopy (SEM) (Phenom Pure G6 Desktop, ThermoFisher, Massachusetts, USA). Prior to observation, the selected fibrous scaffolds were washed twice with PBS, followed by fixation with 4% glutaraldehyde solution (Sigma-Aldrich, St. Louis, USA) at room temperature for 24 h. The scaffolds were washed again with PBS two times and underwent dehydration through a series of graded ethanol solutions (i.e., 30%, 50%, 70%, 90%, and 100%), each for 10 min. The fixed test samples were then dried overnight in a freeze dryer (FreeZone, Labconco, New Hampshire, USA) prior to SEM observation.

Cell viability

The viability of hFOB seeded on all electrospun fibrous scaffolds was evaluated using a fluorescence-based live-dead assay. Two stains were used, namely fluorescein diacetate (FDA) (Sigma Aldrich, Malaysia) and propidium iodide (PI) (Sigma Aldrich, Malaysia) to stain viable and dead hFOB cells, respectively. The staining solution was prepared by mixing FDA, PI and culture medium without FBS at a volume ratio of 8:50:5000. The scaffolds were then stained for 5 min in the dark at room temperature, followed by thrice rinsing with PBS, and immediately scanned using a confocal laser scanning microscope (CLSM) (TCS SP5, Leica, Germany). Similar staining procedures were also performed for cell-seeded TCP prior to viewing via a fluorescence microscope (Eclipse TS100 coupled with Intensilight C-HGFI, Nikon, Japan).

Alkaline phosphatase (ALP) activity

ALP activity of hFOB cultured on different fibrous scaffolds was measured by the ALP assay kit (BioBasic, New York, USA), following the supplier's protocol. The assay kit utilizes para-nitrophenyl phosphate (pNPP), a chromogenic phosphatase substrate that turns yellowish post dephosphorylation by ALP. In brief, 50 µL of cell lysate were incubated with 50 µL phosphatase assay buffer and 50 µL phosphatase substrate for 10 min at room temperature. Subsequently, the absorbance at 405 nm was measured using a microplate reader. The ALP assay was performed in triplicate. The enzymatic activity was calculated according to Eq. (2):

$$\text{Enzymatic activity (nmol/ min)} = \frac{\text{OD}_{405\text{nm}} \times \text{V}}{\varepsilon \times \text{T} \times \text{L}} \times 1000000 \quad (2)$$

where OD_{405nm} is mean absorbance of sample at 405 nm minus mean absorbance of blank at 405 nm, V is reaction volume (L), ε is extinction coefficient of p-nitrophenol (17.8 mM^{-1} cm^{-1}), T is incubation time (min), and L is pathlength of light (cm). L was calculated by dividing reaction volume with surface area of 96-well plate (i.e., 0.32 cm^2).

Statistical analysis

All biocompatibility study data were reported as mean ± SD. One-way analysis of variance (ANOVA) was performed followed by a Tukey's post hoc test to evaluate the significance of the experimental data. The execution of all statistical analyses was made using IBM SPSS (version 23, SPSS Inc., Illinois, USA) software. For *p*-values less than 0.05 ($p < 0.05$), the difference was considered statistically significant.

Results and discussion

Formation of core–shell electrospun fibers

In this study, monolithic PLA and CA, cs-PLA1-CA1, cs-PLA1-CA2, cs-PLA1-CA5, and b-PLA/CA fibers were produced. FESEM micrographs at low and high magnification and D_f distribution of these fibers were shown in Fig. 2, while their respective physical properties were listed in Table 1. Before fabricating PLA-CA core–shell fibers, monolithic PLA and CA fibers were initially produced via

uniaxial electrospinning. For the case of PLA, 12 wt% was demonstrated to be the minimum solution concentration that yields bead-free monolithic PLA fibers in the HFIP system ($D_f = 0.85 \pm 0.21$ µm). Lower solution concentrations of PLA (i.e., 8 wt% and 10 wt%) were shown to lead to the formation of bead-on-string fibers as portrayed in Fig. S1. Similarly, the employment of low solution concentrations of CA (i.e., 4 wt% and 6 wt%) also led to the formation of CA fibers with beads-on-a-string structure, as seen in Fig. S2. In this regard, it was shown that the minimum concentration of CA needed to create beadless monolithic CA fibers with a D_f of 0.84 ± 0.18 µm was 8 wt% (Fig. 2 and Table 1). In both the PLA and CA cases, the formation of beads at low solution concentration (i.e., low viscosity) was speculated to be caused by the insufficient chain entanglements in the solution, which lead to partial jet breakup and eventually the formation of beads or beads-on-a-string fibers [32]. Furthermore, a closer look at high-magnification FESEM micrographs showed that monolithic PLA and CA fibers had different surface morphologies. While the surface of CA fibers has been seen to develop micropores, PLA fibers have a smooth surface. Phase separation was thought to have caused the porous structure of CA as a result of the rapid evaporation of HFIP during uniaxial electrospinning [39, 40].

In order to successfully yield a core–shell structure, several studies have demonstrated that the viscosity of the core solution must be lower than the shell solution [41, 42]. This was to ensure the shell solution is able to guide and confine the core solution to attain core–shell structure [42]. Therefore, for the coaxial electrospinning of PLA-CA, 12 wt% PLA ($\eta = 10.96$ mPa.s) and 8 wt% CA ($\eta = 112.78$ mPa.s) were selected as the core and shell working solutions, respectively, and were injected using three different core-to-shell flow rate ratios; i.e., 0.5:0.5, 0.25:0.5, and 0.1:0.5 mL/hr:mL/hr (designated as cs-PLA1-CA1, cs-PLA1-CA2, and cs-PLA1-CA5, respectively). The flow rate ratio was varied by reducing the core flow rate from 0.5 mL/hr to 0.1 mL/hr, all while maintaining the shell flow rate at 0.5 mL/hr.

From Fig. 2, electrospun fibers with bimodal distribution were observed to be collected during the fabrication of cs-PLA1-CA1. The primary fibers possess a larger average D_f of 1.27 ± 0.20 µm, while the secondary fibers have a smaller average D_f of 0.13 ± 0.02 µm (Table 1). It was postulated that these two distinctive D_f distributions (i.e., bimodal) resulted from secondary jet creation because of jet breakup at a higher core flow rate (i.e., 0.5 mL/hr) [43]. In order to avoid the formation of PLA-CA core–shell fibers with bimodal distribution, the core flow rate was further decreased to 0.25 mL/hr (cs-PLA1-CA2) and 0.1 mL/hr (cs-PLA1-CA5). Initial morphological observation by FESEM revealed the formation of beadless electrospun fibers with normal D_f distribution (Fig. 2 and Table 1). It was also demonstrated that the D_f decreased from 0.99 ± 0.14 µm for cs-PLA1-CA2 to 0.80 ± 0.11 µm for cs-PLA1-CA5. This was understandably due to the lower collective flow rate of cs-PLA1-CA5 (0.1:0.5 mL/hr:mL/hr) compared to cs-PLA1-CA2 (0.25:0.5 mL/hr:mL/hr). In addition, surface pores were also observed on the fiber surface of all collected cs-PLA1-CA1, cs-PLA1-CA2, and cs-PLA1-CA5, with similar surface morphology to monolithic CA fibers. This represents initial confirmation of the successful preparation of PLA-CA core–shell fibers, where smooth PLA was fully confined by the porous outer layer of CA.

In order to confirm the core–shell structure of the cs-PLA-CA fibers, the collected fibers were examined by TEM. Nevertheless, due to the delicate nature of the fibers and the difficulty of separating fibers with a copper grid from the aluminum foil-covered collector, only selective fibers were examined by TEM. In this study, only cs-PLA1-CA2 fibers were selected for TEM due to their relatively high uniformity of D_f distribution and superior mechanical properties compared to cs-PLA1-CA5 and cs-PLA1-CA1 (which will be discussed in detail in Section "Mechanical properties"). As portrayed in Fig. 3, the core–shell structure was clearly observed from the TEM micrograph of cs-PLA1-CA2, with a distinctive core and shell layer. The average diameter of the core layer was 316.54 ± 46.04 nm, while the shell thickness was estimated to be around 256.13 ± 100.48 nm.

For comparison purposes, blend PLA/CA fibers (designated as b-PLA/CA) were also fabricated in this study using uniaxial electrospinning. From Fig. 2, bead-free fibers with smooth surface morphology were collected. The average D_f of b-PLA/CA was 0.88 ± 0.28 µm (Table 1), which is quite close to the average D_f of the other fibers produced in this study. Therefore, a true comparison without the significant influence of D_f variation could be performed.

Apart from D_f, P_f (i.e., the inverse of porosity) and pore size represent other key properties that may influence cell adhesion and infiltration. It is widely reported that low P_f (< 10%) and larger pore size (200–300 µm) result in improved cell viability and infiltration [3]. From Table 1, monolithic PLA possesses the highest P_f (21.64 ± 0.78%) and the lowest pore size (6.97 ± 3.78 µm) among all fibrous scaffolds, which may inhibit cellular adhesion and infiltration due to its lower porosity and small pore size. In addition, the remaining samples show an almost similar P_f between 11.14—11.85%. Monolithic CA, meanwhile, possesses the largest pore size of 13.53 ± 15.25 µm, followed by cs-PLA1-CA2 with a pore size of 11.25 ± 9.70 µm. While these values are far from the desired pore size of 200–300 µm, they are larger than 10 µm which is reported to be the minimum pore size that permits the infiltration of cells into scaffolds [44].

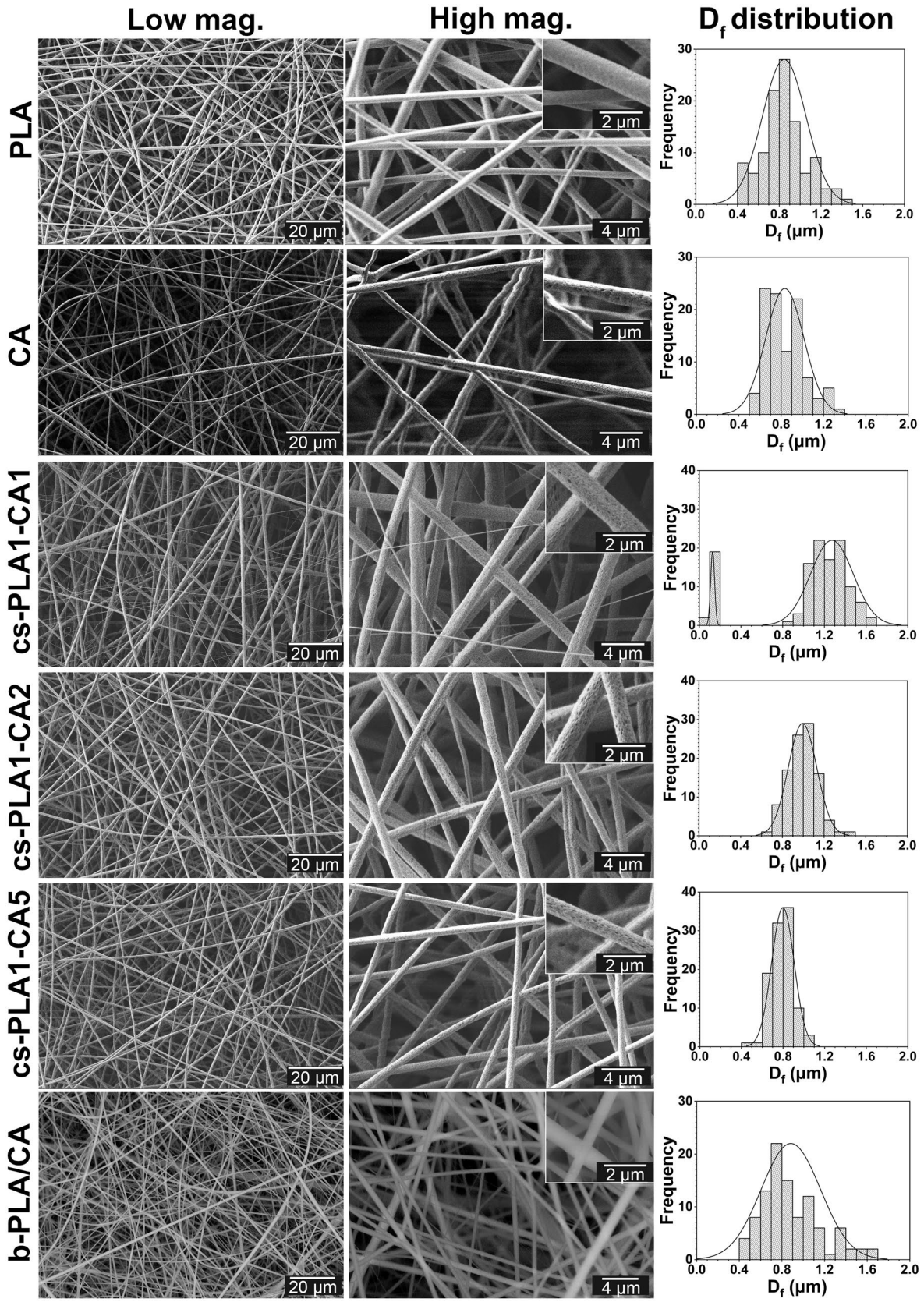

Fig. 2 FESEM micrographs at low (1 kX) and high (4 kX) magnification, and D_f distribution of monolithic PLA and CA, cs-PLA1-CA1, cs-PLA1-CA2, cs-PLA1-CA5, and b-PLA/CA fibers. Very high magnification (8 kX) FESEM micrographs of each sample are shown as inset

Table 1 Physical properties of electrospun fibrous scaffolds produced in this study

Sample	Fiber structure	D_f (μm)	P_f (%)	Pore size (μm)
PLA	Beadless	0.85 ± 0.21	21.64 ± 0.78	6.97 ± 3.78
CA	Beadless	0.84 ± 0.18	11.41 ± 0.91	13.53 ± 15.25
cs-PLA1-CA1	Bimodal	1.27 ± 0.20	11.75 ± 0.73	10.56 ± 12.70
cs-PLA1-CA2	Beadless	0.99 ± 0.14	11.14 ± 0.63	11.25 ± 9.70
cs-PLA1-CA5	Beadless	0.80 ± 0.11	11.38 ± 0.45	8.41 ± 7.58
b-PLA/CA	Beadless	0.88 ± 0.28	11.85 ± 0.35	10.96 ± 12.72

FTIR analysis

Apart from evaluating the surface chemistry and possible chemical interactions between different components in the prepared electrospun fibrous scaffolds, FTIR analysis also can be exploited as an additional tool to confirm the formation of the core–shell structure. In this study, the infrared spectra of monolithic PLA and CA fibers were compared to that of cs-PLA-CA (i.e., cs-PLA1-CA1, cs-PLA1-CA2, cs-PLA1-CA5) and b-PLA/CA (Fig. 4). The FTIR spectrum of monolithic PLA shows a series of peaks which could be assigned to the characteristic peaks of PLA; these include triplet peaks at 1046 cm^{-1}, 1084 cm^{-1}, and 1132 cm^{-1}, and the 1186 cm^{-1} peak which correspond to C—O stretching bands in —O—C═O and —CH—O—, respectively [31], as well as peaks at 1749 cm^{-1}, 1452 cm^{-1}, 868 cm^{-1}, and 758 cm^{-1} which could be assigned to C═O stretching of PLA, CH_3 symmetric deformation vibration [45], C—COO stretching, and δC═O in-plane bending [46], respectively. Meanwhile, a significant broad peak was observed at 3475 cm^{-1} from the FTIR spectrum of monolithic CA which can be assigned to the —OH stretching of hydroxyl groups in CA [29]. Several other characteristic peaks of CA were also observed from the CA spectrum including peaks at 1744 cm^{-1}, 1371 cm^{-1}, 1236 cm^{-1}, and 1037 cm^{-1} which correspond to C═O stretching of carbonyl (acetyl) group, symmetric —C—H bending vibration of —CH_3 in acetyl, asymmetric stretching of C—O—C bond of the ester group in the glycosidic linkage of CA, and C—O—C of cellulose backbone, respectively [31, 47, 48]. Two more peaks with low intensity were also detected at 1646 cm^{-1} and 906 cm^{-1} which indicate the presence of water molecules (H—OH) and CH_2 rocking vibrations, respectively [49].

In the case of cs-PLA1-CA1, the strong intensity of PLA peaks at 1749 cm^{-1}, 1186 cm^{-1}, and 1084 cm^{-1} can still be observed from the FTIR spectrum, confirming the fact that the PLA-core penetrated to the outer layer during coaxial electrospinning and remained at the surface of the fibrous scaffold. The intensity of these characteristic peaks of PLA became smaller in the spectra of cs-PLA1-CA2 and cs-PLA1-CA5, while the intensity of typical CA peaks at 1037 cm^{-1}, 1236 cm^{-1}, 1371 cm^{-1}, and 3475 cm^{-1} was getting clearer and higher. This could give another indication that the PLA-core has been successfully confined by the CA-shell in cs-PLA1-CA2 and cs-PLA1-CA5. On the other hand, the FTIR spectrum of b-PLA/CA consisted mostly of the peaks of both PLA and CA at different intensities, which suggests the presence of both materials at the surface of the composite fibers. Specifically, the broad peak at 3475 cm^{-1} was still observed in the FTIR spectrum of

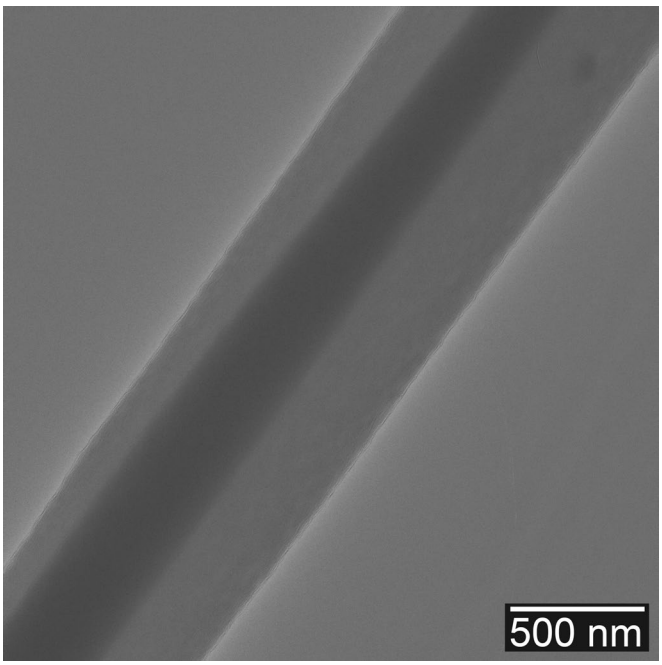

Fig. 3 TEM micrograph of cs-PLA1-CA2

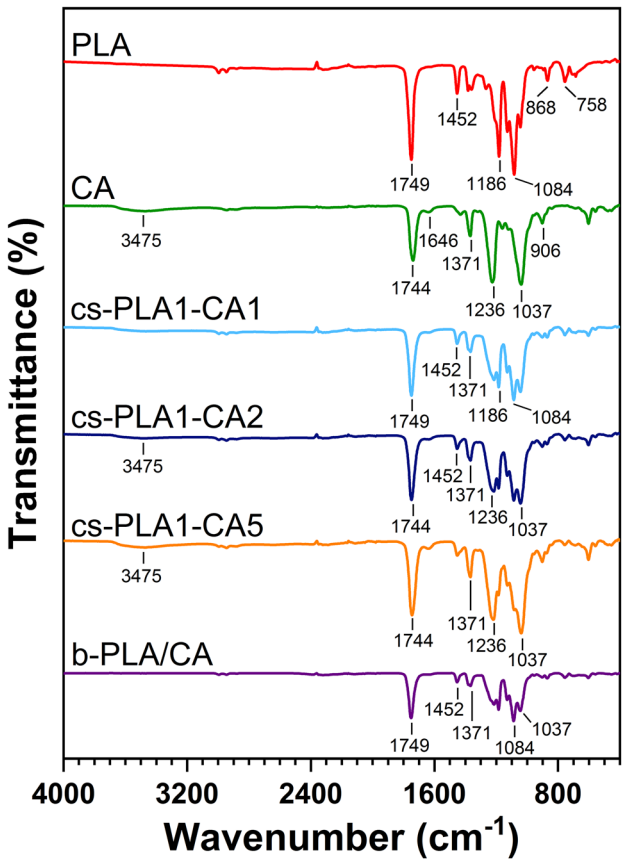

Fig. 4 FTIR spectra of monolithic PLA and CA, cs-PLA-CA, and b-PLA/CA electrospun fibers

b-PLA/CA, albeit with reduced intensity compared to that of pure CA. This could be attributed to the existence of hydrogen bonding between the ─OH of CA and the ester ─C═O of PLA, resulting in the intensity reduction of the corresponding infrared peak. Such results demonstrate the existence of secondary interactions between CA and PLA chains [29].

Mechanical properties

Apart from the all-important osteoconductivity, the mechanical properties of fibrous scaffolds represent another key criterion to ensure successful application in bone tissue engineering. The typical effective stress–strain curves of monolithic PLA and CA, all cs-PLA-CA, and b-PLA/CA fibers were shown in Fig. 5, while their tensile properties were summarized in Table 2. In comparing monolithic PLA and CA fibers, the results clearly demonstrate the weak tensile properties of CA compared to PLA fibers. From Table 2, monolithic CA was shown to possess the lowest ultimate tensile strength (UTS) and Young's modulus of 8.43 ± 1.27 MPa and 0.24 ± 0.03 GPa, respectively, while showing moderate elongation at break of $12.46 \pm 1.53\%$. On the contrary, monolithic PLA demonstrates relatively higher tensile strength (18.02 ± 1.68 MPa), stiffness (0.60 ± 0.02 GPa), and elongation at break ($83.08 \pm 20.94\%$) than monolithic CA. It was evident from these results that the incorporation of PLA was needed to improve the overall tensile properties of CA-based fibrous scaffolds. The tensile data for monolithic PLA and CA reported in this study were observed to be higher than the values reported in other studies [20, 50]. The reason for this difference could be due to the exclusion of the porosity factor (which can go up to 90%) of the fibrous scaffolds during tensile evaluation in previous studies. Following a similar method as in our recently published work [32], the effective cross-section, which is

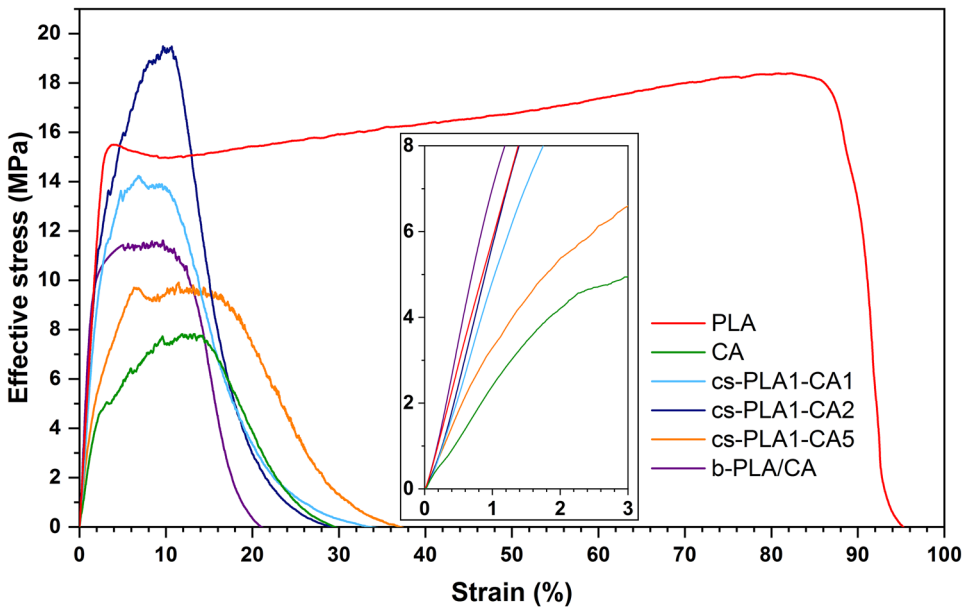

Fig. 5 Typical effective stress–strain curve of monolithic PLA and CA, cs-PLA-CA, and b-PLA/CA fibers. Enlarged plot of the curve in elastic region is shown as inset

Table 2 Tensile properties of monolithic PLA and CA, cs-PLA-CA, and b-PLA/CA electrospun fibers. All values represent mean ± SD from at least 5 tensile specimens for each sample. Tensile data for native cancellous bone is also provided as comparison

Sample	UTS (MPa)	Young's modulus (GPa)	Elongation at break (%)
PLA	18.02 ± 1.68	0.60 ± 0.02*	83.08 ± 20.94
CA	8.43 ± 1.27	0.24 ± 0.03*	12.46 ± 1.53
cs-PLA1-CA1	14.35 ± 0.55	0.52 ± 0.05*	7.99 ± 1.63
cs-PLA1-CA2	19.53 ± 1.68	0.62 ± 0.09*	10.24 ± 1.70
cs-PLA1-CA5	9.80 ± 2.02	0.32 ± 0.05*	7.73 ± 2.15
b-PLA/CA	12.42 ± 0.92	0.74 ± 0.02*	10.39 ± 1.32
Native cancellous bone [51]	10–20	0.05–0.5	5–7
Native cortical bone [51]	50–150	7–30	1–3

*Young's modulus was calculated at 0.2—1% strain

the multiplication of the initial cross-section of fibrous scaffold with the respective P_f was used in the calculation of effective stress. In our opinion, the effective stress embodies a more accurate interpretation of the true tensile values of a porous fibrous scaffold.

The overall tensile properties of PLA-CA core–shell fibers are expected to be significantly influenced by the fiber structure, D_f, and weight fraction of the core and shell components. From Table 2, cs-PLA1-CA2 was revealed to possess the highest UTS (19.53 ± 1.68 MPa), Young's modulus (0.62 ± 0.09 GPa), and elongation at break (10.24 ± 1.70%) among all PLA-CA core–shell fibers evaluated in this study. This was followed by cs-PLA1-CA1 with an UTS of 14.35 ± 0.55 MPa, Young's modulus of 0.52 ± 0.05 GPa, and elongation at break of 7.99 ± 1.63%. The decreased tensile properties of cs-PLA1-CA1 were speculated to be caused by the bimodal distribution and larger D_f compared to cs-PLA1-CA2. It is widely accepted that a smaller D_f usually results in higher tensile properties for defect-free electrospun fibers [52]. Meanwhile, cs-PLA1-CA5 was shown to have the weakest tensile properties among all cs-PLA-CA (UTS of 9.80 ± 2.02 MPa, stiffness of 0.32 ± 0.05 GPa, and elongation at break of 7.73 ± 2.15%) despite possessing the smallest D_f (0.80 ± 0.11 µm). This shows that the weight fraction of components in core–shell fibers also plays an important role in affecting their mechanical properties; for the case of cs-PLA1-CA5, the weight fraction of PLA-core was expected to be lower due to the smaller flow rate ratio of PLA-to-CA during coaxial electrospinning (i.e., PLA-core to CA-shell flow rate ratio is 0.1:0.5 mL/hr:mL/hr for cs-PLA1-CA5). Therefore, the lesser weight fraction of PLA and vice versa, the higher weight fraction of CA in cs-PLA1-CA5 might lead to these reduced tensile properties owing to the lower mechanical contribution by the PLA-core.

As the best PLA-CA core–shell fibers with the highest tensile properties, cs-PLA1-CA2 was compared to its monolithic fiber counterparts. cs-PLA1-CA2 displays a 130% increase in UTS and a 160% increase in Young's modulus, while showing a nearly 18% reduction in elongation at break as compared to monolithic CA. The same goes for comparison with monolithic PLA; cs-PLA1-CA2 demonstrates around 8% and nearly 4% increase in UTS and Young's modulus but exhibits a massive 87% reduction in elongation at break. This observation was not uncommon, as the increase in tensile strength and stiffness is typically accompanied by a decrease in strain at failure [9]. Meanwhile, b-PLA/CA was shown to possess inferior UTS (12.42 ± 0.92 MPa) and slightly higher elongation at break (10.39 ± 1.32%) compared to cs-PLA1-CA2. However, b-PLA/CA was revealed to have the highest elastic modulus of 0.74 ± 0.02 GPa among all evaluated fibrous scaffolds, highly likely due to the existence of secondary interactions between CA and PLA chains, as described in FTIR results earlier.

To put these tensile values into perspective for the targeted application, the comparison was made against native bones (i.e., cancellous bone and cortical bone). The tensile data revealed that the cs-PLA1-CA2 is suitable and matches the mechanical criteria of native cancellous bone but may not be appropriate for use in denser-type of bones (cortical). While PLA and b-PLA/CA also demonstrate the mechanical suitability of native cancellous bone, the presence of less biocompatible PLA on their surfaces may inhibit their applications in bone tissue engineering.

Thermal analysis and degree of crystallinity

Figure 6 depicts the first scan heating DSC thermograms of monolithic PLA and CA, all cs-PLA-CA, b-PLA/CA, as well as PLA granules and CA powder. In addition, their important thermal properties, including T_g, T_m, T_{cc}, T_{mc}, and X_c were summarized in Table S1. From the DSC thermogram of PLA, two endothermic peaks including double melting points were observed, which correspond to T_g and T_m. The T_g of PLA (65.94 °C) was revealed to be lower than the T_g of as-received PLA granules (69.89 °C). Furthermore, double T_m was observed at two varying temperatures, with the first melting point at 173.84 °C and the second point at 177.84 °C. This can be attributed to the melting of the original PLA crystals and the melting of the recrystallized

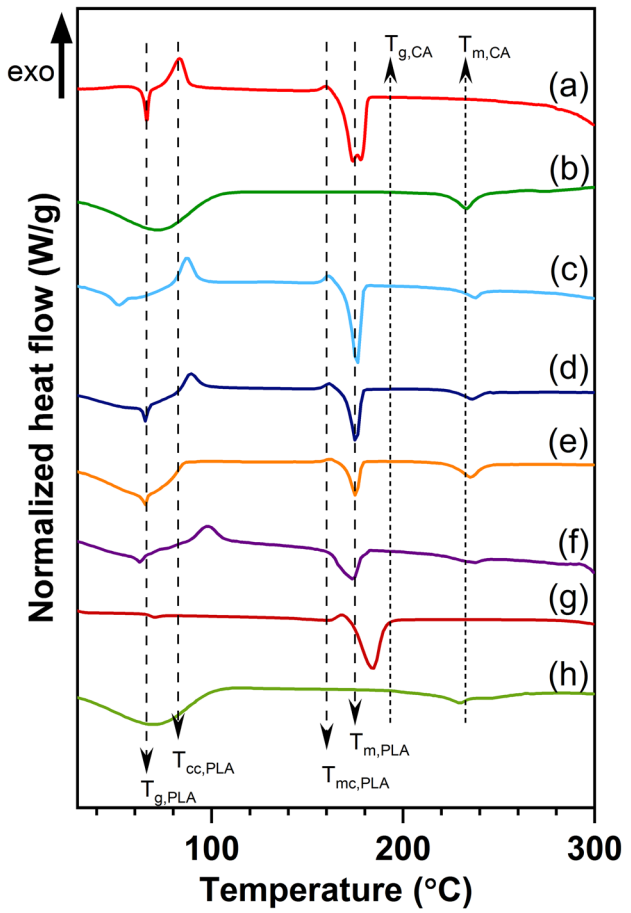

Fig. 6 First scan heating DSC thermograms of **a** PLA, **b** CA, **c** cs-PLA1-CA1, **d** cs-PLA1-CA2, **e** cs-PLA1-CA5, **f** b-PLA/CA, and as-received **g** PLA granule and **h** CA powder

crystals produced through melt-recrystallization during the heating scan, respectively [53]. Both of these T_m values, however, were also lower compared to the T_m of PLA granules (184.74 °C). The inferior T_g and T_m values of PLA fibers in comparison to bulk PLA granules have also been reported previously [32]. The $T_{g,PLA}$ and $T_{m,PLA}$ of cs-PLA1-CA1, cs-PLA1-CA2, cs-PLA1-CA5, and b-PLA/CA were also revealed to be lower than those of PLA granules. These decreases could be attributed to the enhanced mobility of PLA segments owing to reduced chain entanglements and a larger fiber surface-to-volume ratio [54].

When comparing the $X_{c,PLA}$ of all fibrous scaffolds containing PLA, the crystallinity was revealed to be higher (e.g., cs-PLA1-CA2, and cs-PLA1-CA5) and lower (e.g., monolithic PLA, cs-PLA1-CA1, and b-PLA/CA) than that of PLA granules. The lower PLA crystallinity of monolithic PLA, cs-PLA1-CA1, and b-PLA/CA was speculated to be caused by the destruction of the initial PLA crystals during dissolution and rapid solidification of the polymeric chains during electrospinning, which prevent the re-formation of the PLA crystals [55]. Contradictory results were observed for cs-PLA1-CA2 and cs-PLA1-CA5. Their PLA crystallinity was revealed to be higher than PLA granules. This observation may result from the improved molecular chain orientation provided by the CA-shell during coaxial electrospinning. This was in agreement with the observation reported by Merkle and coworkers [56]. The elasticity of CA was hypothesized to suppress the Rayleigh instability of the PLA-core, whereby the higher degree of molecular chain orientation of PLA was induced. Specifically, the CA-shell solution acts as a "shield" to protect the PLA-core from the turbulent surface during coaxial electrospinning, which allows the PLA chains to be stretched further and better oriented, resulting in higher crystallinity, as was observed for cs-PLA1-CA2 and cs-PLA1-CA5 (Table S1). This was speculated to contribute to the improved tensile strength and stiffness of cs-PLA1-CA2. While the crystallinity of PLA is the highest in cs-PLA1-CA5 (76.58%), this was not reflected in superior tensile properties of cs-PLA1-CA5, highly likely due to a reduced weight fraction of PLA component owing to a lower PLA flow rate (i.e., 0.1 mL/hr) as discussed earlier in the tensile results.

Lastly, the crystallinity of PLA in b-PLA/CA (19.80%) was observed to be lower than that of monolithic PLA, cs-PLA1-CA1, cs-PLA1-CA2, and cs-PLA1-CA5, despite demonstrating the highest elastic modulus among them. This observation was highly likely due to the decreased crystallization of PLA as a result of reduced molecular chain mobility and flexibility caused by the relatively high viscosity of CA solution.

Cell proliferation

As cs-PLA1-CA2 has achieved submicron size and possesses the highest tensile properties among all PLA-CA core–shell fibers produced in this study, cs-PLA1-CA2 was considered to be the best PLA-CA core–shell fibers and was selected for biocompatibility comparison with its monolithic fiber counterparts (i.e., PLA and CA), b-PLA/CA, and TCP as a control. In this study, an AB assay was used to assess the cell proliferation on different scaffold surfaces. The total percentage of AB reduction for all samples at different time points (up to 14 days) is shown in Fig. 7.

The AB assay revealed that cs-PLA1-CA2 had the highest percentage of AB reduction for all time points with significant difference to PLA and b-PLA/CA samples ($p < 0.05$), indicating improved cell proliferation with the inclusion of CA-shell layer in cs-PLA1-CA2. This can be explained by the presence of hydroxyl moieties in the CA backbone, which results in better stimulation of the binding between the cell and the surface of cs-PLA1-CA2. Nevertheless, no significant difference ($p > 0.05$) of AB reduction was observed between cs-PLA1-CA2 with CA and TCP

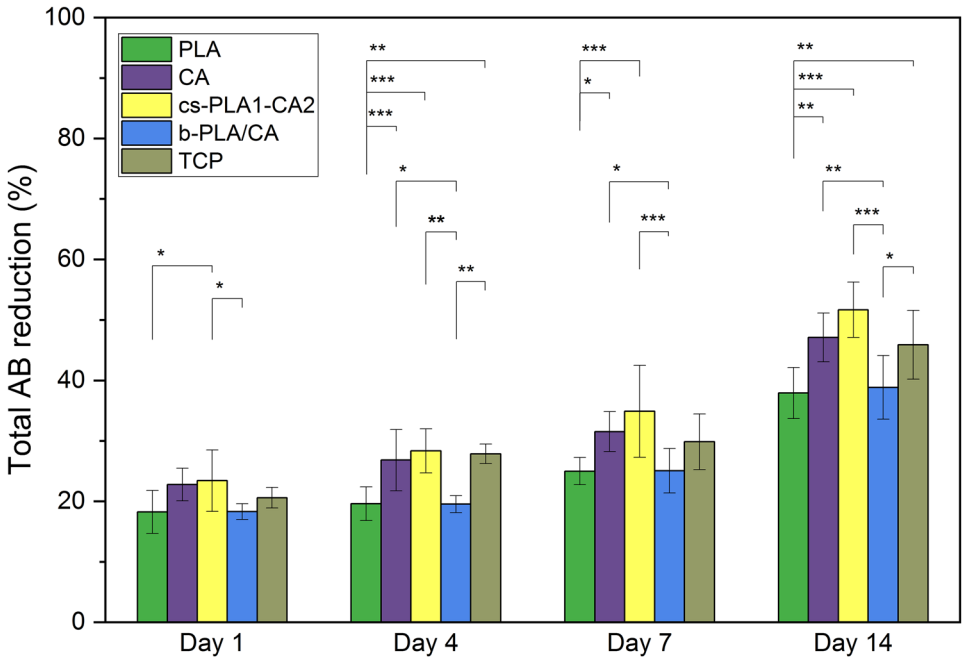

Fig. 7 AB proliferation results of hFOB grown on PLA, CA, cs-PLA1-CA2, and b-PLA/CA, in comparison to the control (TCP). The asterisks indicate statistically significant difference; * $p < 0.05$, ** $p < 0.01$, and *** $p < 0.001$

during 14 days of culture, which signifies the similar level of osteoconductivity between cs-PLA1-CA2, CA, and two-dimensional (2D) TCP. Despite showing lower AB reduction compared to cs-PLA1-CA2 and CA, the cellular proliferation on PLA and b-PLA/CA scaffolds was observed to show a continual increasing trend from day 1 to day 14, which suggests that PLA-based scaffolds are non-toxic and could still support the proliferation of hFOB cells. The presence of CA in b-PLA/CA scaffold resulted in slightly higher AB reduction compared to PLA scaffold after 14 days; however, the results were not statistically significant ($p = 0.99$).

Cell viability and morphology

The cellular morphology, spreading, and viability on the fibrous scaffolds were assessed by SEM and CLSM, respectively for up to 7 days-incubation period. The SEM micrographs of hFOB cultured on PLA, CA, cs-PLA1-CA2, and b-PLA/CA on different days were shown in Fig. 8. While the hFOB cells were observed to adhere to all fibrous surfaces, the cells are seen to be more stretched and well-anchored to the cs-PLA1-CA2 and CA fibers through distinct filopodia [57], compared to PLA and b-PLA/CA scaffolds. In addition, the cells seeded on cs-PLA1-CA2, and CA scaffolds were also observed to proliferate well in the direction of the fiber alignment while forming many adhesion sites with the underlying scaffolds. In contrast, the hFOB cells were observed to be flattened and thicker

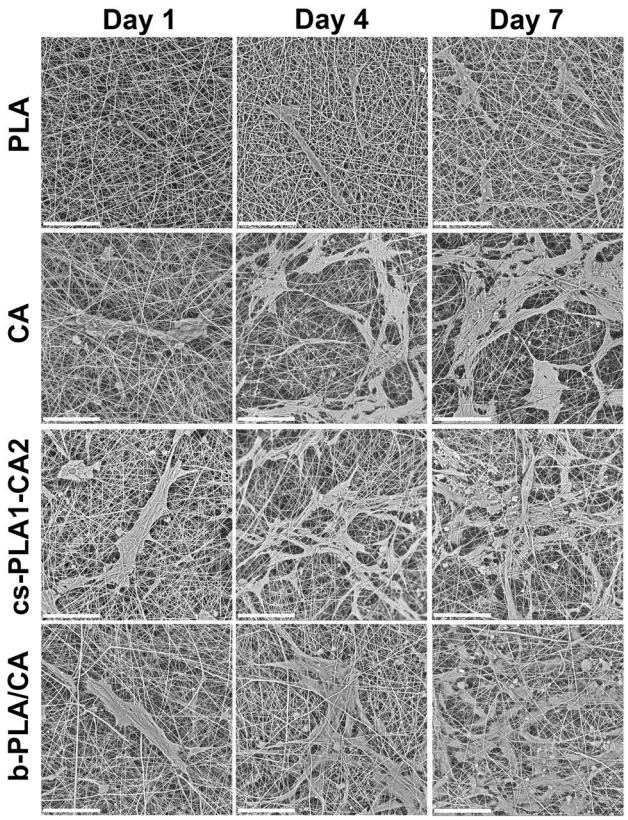

Fig. 8 SEM micrographs of hFOB seeded on PLA, CA, cs-PLA1-CA2, and b-PLA/CA on different days. The scale bar is 80 µm

with less distinct filopodia in day 7 of cultivation on PLA and b-PLA/CA scaffolds, although the cell spreading on the b-PLA/CA scaffold was visibly larger than the cell spreading on the PLA scaffold. This was in line with the cell proliferation results, which indicate the lack of cell adhesion sites on PLA-containing surfaces.

Meanwhile, the cellular viability of hFOB for incubation period of 7 days was assessed by live-dead assay using FDA and PI to indicate viable and dead cells, respectively. The live-dead CLSM images of hFOB cultured on PLA, CA, cs-PLA1-CA2, and b-PLA/CA at different time points were portrayed in Fig. 9. The live-dead fluorescence microscope images of hFOB seeded on TCP were also shown as comparison. From Fig. 9, it can be revealed that all scaffolds (i.e., PLA, CA, cs-PLA1-CA2 and b-PLA/CA) evaluated in this study are capable to support the growth of hFOB cells on their surfaces, as demonstrated by the increasing green spots from day 1 to day 7 indicating higher cell population from the initial seedings. Nevertheless, the cell density and morphology are visibly different for cells cultured on cs-PLA1-CA2 and CA, compared to those cultivated on PLA and b-PLA/CA. The hFOB cells were evidently exhibited higher cell density on cs-PLA1-CA2 and CA scaffolds especially after 4-days and 7-days incubation, where the cells were shown to be well-stretched with extended filopodia which epitomizes the typical morphology of osteoblast cells [58].

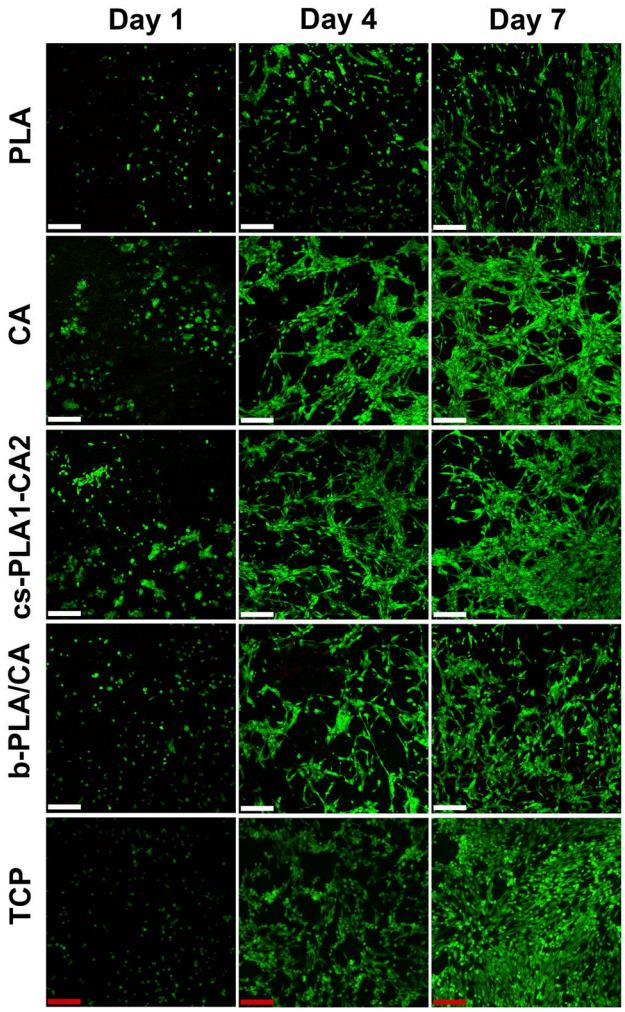

Fig. 9 Live-dead CLSM images of hFOB seeded on PLA, CA, cs-PLA1-CA2, and b-PLA/CA at different time points. (Fifth row) Live-dead fluorescence microscope images of hFOB cultured on TCP on different days as comparison. Green indicated viable cells, while red showed dead cells. The white scale bar is 200 µm, while the red scale bar is 20 µm

In comparing cs-PLA1-CA2 and CA fibers, the cells could be observed to have better penetration and infiltration into the cs-PLA1-CA2 compared to CA fibers, despite the fact that CA (13.53 ± 15.25 µm) has a larger pore size than cs-PLA1-CA2 (11.25 ± 9.70 µm). This indication of cell penetration can be represented by the z-stack range of the sample during CLSM imaging (Fig. S3). Better cell penetration in cs-PLA1-CA2 was observed in response to the superior stiffness and strength of the underlying fibrous scaffold, in agreement with the observation by Merkle et al. [7]. On the other hand, the cells seeded on PLA and b-PLA/CA scaffolds were observed to grow more individually, where the cells spread out and occupied a wider space by day 4. This observation was similar to the state of hFOB cells cultivated on 2D TCP, as shown in Fig. 9, albeit with significantly lower cell density compared to TCP. The similar characteristic morphology of hFOB cells cultured on 2D TCP was also previously reported by Ghag et al. [59].

Alkaline phosphatase (ALP) activity

The ALP activity designates the presence of osteoblasts and could serve as an early indication of new bone formation [60]. Figure 10 shows the ALP activity of hFOB cells grown on different electrospun fibrous scaffolds (i.e., PLA, CA, cs-PLA1-CA2, and b-PLA/CA), in comparison to the control (TCP), over an incubation period of 14 days. For all evaluated fibrous scaffolds, the ALP activity showed an increasing trend from day 1 until day 14. The highest ALP activity was observed for cs-PLA1-CA2 at all time points, which includes the comparison to TCP, confirming the result of AB reduction as discussed earlier. The ALP activity of cs-PLA1-CA2 was significantly different ($p < 0.05$) from the ALP activity measured for PLA and b-PLA/CA scaffolds on day 1, 4 and 7; for day 14, the ALP activity of cs-PLA1-CA2 was significantly different ($p < 0.05$) only from PLA fibers. In addition, the ALP activity of cs-PLA1-CA2 and CA scaffolds was demonstrated to be higher than TCP at all evaluated time points, which could indicate that the CA surfaces and 3D fibrous network favor the expression of enzymatic activity of hFOB, in agreement to the observation by Atila et al. [17].

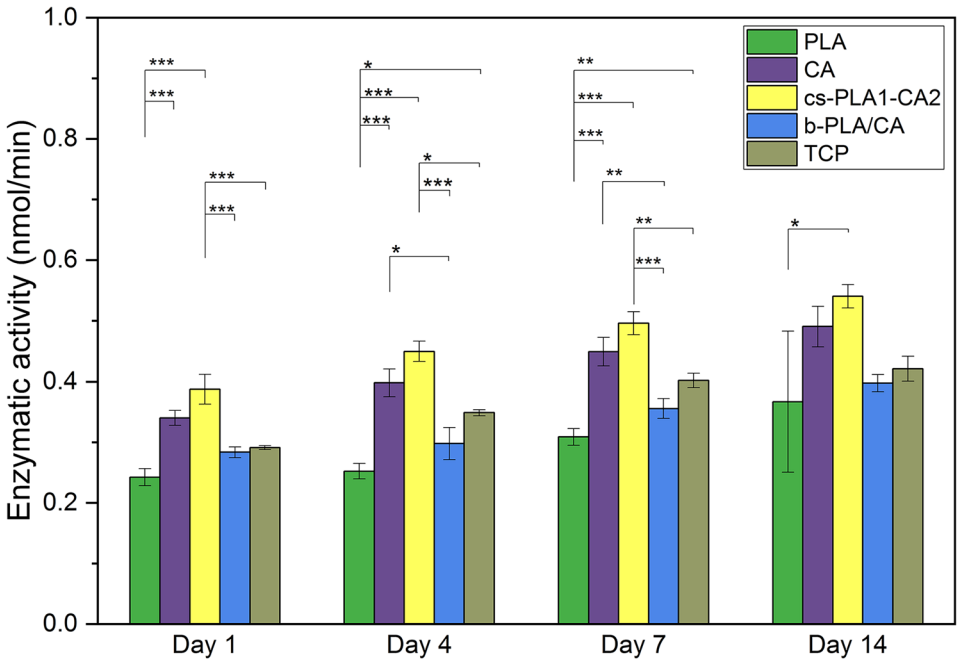

Fig. 10 ALP activity of hFOB cells grown on PLA, CA, cs-PLA1-CA2, and b-PLA/CA, in comparison to the control (TCP) at different time points. The asterisks indicate statistically significant difference; * $p < 0.05$, ** $p < 0.01$, and *** $p < 0.001$

Conclusions

In this study, we sought to assess the potential of PLA-CA core–shell fibers for bone tissue engineering. It was hypothesized that the employment of PLA as the core and CA as the shell component would improve the mechanical properties and bioactivity of the core–shell fibers in comparison to monolithic PLA or CA fibers. According to FESEM and TEM images, FTIR spectra, and tensile studies, 0.25:0.5 mL/hr:mL/hr (referred to as cs-PLA1-CA2) is the optimal core-to-shell flow rate ratio that results in core–shell fibers with uniform D_f, and the maximum tensile strength and stiffness among all examined cs-PLA-CA. Further thermal analysis indicates the improved crystallinity and higher weight fraction of PLA-core to be the key factors in the mechanical enhancement of cs-PLA1-CA2. Interestingly, the tensile data revealed that the cs-PLA1-CA2 is suitable and matches the mechanical criteria of native cancellous bone but may not be appropriate for usage in denser-type of bones (e.g., cortical). In comparison to monolithic PLA and b-PLA/CA scaffolds, the inclusion of CA-shell as the surface layer of cs-PLA1-CA2 has led to better cell-scaffold interaction, as demonstrated by higher cell proliferation, better cell spreading, and higher cell density and ALP activity over the course of the incubation period. Overall, the PLA-CA core–shell fibers (cs-PLA1-CA2) produced in this study exhibit excellent tensile properties while supporting the growth and attachment of human osteoblastic cell-lines, indicating the scaffold's promising potential for use in bone tissue engineering applications.

Supplementary Information The online version contains supplementary material available at https://doi.org/10.1007/s10965-023-03639-0.

Acknowledgements The authors were grateful for the research funding for this work from the Fundamental Research Grant Scheme (FRGS), Ministry of Higher Education (MOHE), Malaysia (grant no. FP048-2019 A). M. F. Abdullah also acknowledges the financial support from MOHE, Malaysia and Universiti Malaysia Perlis through the "Skim Latihan Akademik Bumiputera (SLAB)" program. The authors would also like to thank Liyana Abu and Kelvin Ng for the technical support and valuable advice that they provided during cell culture experiments.

Data availability The raw data of this study are available from the corresponding authors upon reasonable request.

Declarations

Conflict of interest The authors declare that they have no known competing financial interests or personal relationships that could have appeared to influence the work reported in this paper.

References

1. Guo BL, Ma PX (2018) Conducting Polym Tissue Eng Biomacromolecules 19:1764–1782
2. Haider A, Haider S, Kang I-K (2015) A comprehensive review summarizing the effect of electrospinning parameters and potential applications of nanofibers in biomedical and biotechnology. Arab J Chem 11:1165–1188
3. Narayanan G, Vernekar VN, Kuyinu EL, Laurencin CT (2016) Poly (lactic acid)-based biomaterials for orthopaedic regenerative engineering. Adv Drug Deliver Rev 107:247–276
4. Abdullah MF, Nuge T, Andriyana A, Ang BC, Muhamad F (2019) Core-shell fibers: design, roles, and controllable release strategies in tissue engineering and drug delivery. Polymers 11:2008

5. Sperling LE, Reis KP, Pranke P, Wendorff JH (2016) Advantages and challenges offered by biofunctional core-shell fiber systems for tissue engineering and drug delivery. Drug Discov Today 21:1243–1256
6. Atila D, Hasirci V, Tezcaner A (2022) Coaxial electrospinning of composite mats comprised of core/shell poly(methyl methacrylate)/silk fibroin fibers for tissue engineering applications. J Mech Behav Biomed Mater 128:105105
7. Merkle VM, Tran PL, Hutchinson M, Ammann KR, DeCook K, Wu X, Slepian MJ (2015) Core–shell PVA/gelatin electrospun nanofibers promote human umbilical vein endothelial cell and smooth muscle cell proliferation and migration. Acta Biomater 27:77–87
8. Gregor A, Filova E, Novak M, Kronek J, Chlup H, Buzgo M, Blahnova V, Lukasova V, Bartos M, Necas A, Hosek J (2017) Designing of PLA scaffolds for bone tissue replacement fabricated by ordinary commercial 3D printer. J Biol Eng 11:31
9. Alharbi HF, Luqman M, Khalil KA, Elnakady YA, Abd-Elkader OH, Rady AM, Alharthi NH, Karim MR (2018) Fabrication of core-shell structured nanofibers of poly (lactic acid) and poly (vinyl alcohol) by coaxial electrospinning for tissue engineering. Eur Polym J 98:483–491
10. Schroepfer M, Junghans F, Voigt D, Meyer M, Breier A, Schulze-Tanzil G, Prade I (2020) Gas-phase fluorination on PLA improves cell adhesion and spreading. ACS Omega 5:5498–5507
11. Cai ZJ, Yi X, Yang HZ, Jia JR, Liu YP (2016) Poly(hydroxybutyrate)/cellulose acetate blend nanofiber scaffolds: Preparation, characterization and cytocompatibility. Mater Sci Eng C-Mater Biol Appl 58:757–767
12. Golizadeh M, Karimi A, Gandomi-Ravandi S, Vossoughi M, Khafaji M, Joghataei MT, Faghihi F (2019) Evaluation of cellular attachment and proliferation on different surface charged functional cellulose electrospun nanofibers. Carbohydr Polym 207:796–805
13. Quan ZZ, Wang YH, Wu JJ, Qin XH, Yu JY (2021) Preparation and characterization of electrospun cellulose acetate sub-micro fibrous membranes. Text Res J 91:2540–2550
14. Samadian H, Salehi M, Farzamfar S, Vaez A, Ehterami A, Sahrapeyma H, Goodarzi A, Ghorbani S (2018) In vitro and in vivo evaluation of electrospun cellulose acetate/gelatin/hydroxyapatite nanocomposite mats for wound dressing applications. Artif Cell Nanomed Biotechnol 46:S964–S974
15. Cheng HN, Dowd MK, Selling GW, Biswas A (2010) Synthesis of cellulose acetate from cotton by products. Carbohydr Polym 80:449–452
16. Khoshnevisan K, Maleki H, Samadian H, Shahsavari S, Sarrafzadeh MH, Larijani B, Dorkoosh FA, Haghpanah V, Khorramizadeh MR (2018) Cellulose acetate electrospun nanofibers for drug delivery systems: applications and recent advances. Carbohydr Polym 198:131–141
17. Atila D, Keskin D, Tezcaner A (2016) Crosslinked pullulan/cellulose acetate fibrous scaffolds for bone tissue engineering. Mater Sci Eng C-Mater Biol Appl 69:1103–1115
18. Ertas Y, Uyar T (2017) Fabrication of cellulose acetate/polybenzoxazine cross-linked electrospun nanofibrous membrane for water treatment. Carbohydr Polym 177:378–387
19. Teixeira MA, Antunes JC, Seabra CL, Tohidi SD, Reis S, Amorim MTP, Felgueiras HP (2022) Tiger 17 and pexiganan as antimicrobial and hemostatic boosters of cellulose acetate-containing poly(vinyl alcohol) electrospun mats for potential wound care purposes. Int J Biol Macromol 209:1526–1541
20. Sinha R, Janaswamy S, Prasad A (2020) Enhancing mechanical properties of Electrospun cellulose acetate Fiber mat upon Potassium Chloride exposure. Materialia 14:100881
21. Lee J, Moon JY, Lee JC, Hwang TI, Park CH, Kim CS (2021) Simple conversion of 3D electrospun nanofibrous cellulose acetate into a mechanically robust nanocomposite cellulose/calcium scaffold. Carbohydr Polym 253:117191
22. Liguori A, Bigi A, Colombo V, Focarete ML, Gherardi M, Gualandi C, Oleari MC, Panzavolta S (2016) Atmospheric pressure Non-Equilibrium plasma as a Green Tool to Crosslink gelatin nanofibers. Sci Rep 6:38542
23. Ma B, Wang X, Wu C, Chang J (2014) Crosslinking strategies for preparation of extracellular matrix-derived cardiovascular scaffolds. Regen Biomater 1:81–89
24. Song KL, Xu HL, Mu BN, Xie KL, Yang YQ (2017) Non-toxic and clean crosslinking system for protein materials: Effect of extenders on crosslinking performance. J Clean Prod 150:214–223
25. Stone SA, Gosavi P, Athauda TJ, Ozer RR (2013) In situ citric acid crosslinking of alginate/polyvinyl alcohol electrospun nanofibers. Mater Lett 112:32–35
26. Chang A, Ye Z, Ye Z, Deng J, Lin J, Wu C, Zhu H (2022) Citric acid crosslinked sphingan WL gum hydrogel films supported ciprofloxacin for potential wound dressing application. Carbohydr Polym 291:119520
27. Zhao W, Cao S, Cai H, Wu Y, Pan Q, Lin H, Fang J, He Y, Deng H, Liu Z (2022) Chitosan/silk fibroin biomimic scaffolds reinforced by cellulose acetate nanofibers for smooth muscle tissue engineering. Carbohydr Polym 298:120056
28. Elsayed RE, Madkour TM, Azzam RA (2020) Tailored-design of electrospun nanofiber cellulose acetate/poly(lactic acid) dressing mats loaded with a newly synthesized sulfonamide analog exhibiting superior wound healing. Int J Biol Macromol 164:1984–1999
29. Gomaa SF, Madkour TM, Moghannem S, El-Sherbiny IM (2017) New polylactic acid/ cellulose acetate-based antimicrobial interactive single dose nanofibrous wound dressing mats. Int J Biol Macromol 105:1148–1160
30. Chen J, Zhang T, Hua W, Li P, Wang X (2020) 3D porous poly(lactic acid)/regenerated cellulose composite scaffolds based on electrospun nanofibers for biomineralization. Colloid Surf A-Physicochem Eng Asp 585:124048
31. Naseri-Nosar M, Salehi M, Hojjati-Emami S (2017) Cellulose acetate/poly lactic acid coaxial wet-electrospun scaffold containing citalopram-loaded gelatin nanocarriers for neural tissue engineering applications. Int J Biol Macromol 103:701–708
32. Abdullah MF, Andriyana A, Muhamad F, Ang BC (2021) Effect of core-to-shell flowrate ratio on morphology, crystallinity, mechanical properties and wettability of poly(lactic acid) fibers prepared via modified coaxial electrospinning. Polymer 237:124378
33. Joy N, Samavedi S (2020) Identifying specific combinations of matrix properties that promote controlled and sustained release of a hydrophobic drug from electrospun meshes. ACS Omega 5:15865–15876
34. Davachi SM, Kaffashi B (2015) Preparation and characterization of poly L-Lactide/Triclosan nanoparticles for specific antibacterial and medical applications. Int J Polym Mater Polym Biomat 64:497–508
35. Fischer EW, Sterzel HJ, Wegner G (1973) Investigation of the structure of solution grown crystals of lactide copolymers by means of chemical reactions. Kolloid-Zeitschrift und Zeitschrift für Polymere 251:980–990
36. Jia SK, Yu DM, Zhu Y, Wang Z, Chen LG, Fu L (2017) Morphology, crystallization and thermal behaviors of PLA-based composites: wonderful effects of hybrid GO/PEG via dynamic impregnating. Polymers 9:528
37. Hassan M, Berglund L, Abou-Zeid R, Hassan E, Abou-Elseoud W, Oksman K (2019) Nanocomposite Film based on cellulose acetate and Lignin-Rich Rice Straw Nanofibers. Materials 12:595
38. Cerqueira DA, Rodrigues Filho G, Assunção RMN (2006) A New Value for the heat of Fusion of a perfect crystal of cellulose acetate. Polym Bull 56:475–484

39. Celebioglu A, Uyar T (2011) Electrospun porous cellulose acetate fibers from volatile solvent mixture. Mater Lett 65:2291–2294
40. Han SO, Son WK, Youk JH, Lee TS, Park WH (2005) Ultrafine porous fibers electrospun from cellulose triacetate. Mater Lett 59:2998–3001
41. Khalf A, Singarapu K, Madihally SV (2015) Cellulose acetate core-shell structured electrospun fiber: fabrication and characterization. Cellulose 22:1389–1400
42. Jalvo B, Mathew AP, Rosal R (2017) Coaxial poly(lactic acid) electrospun composite membranes incorporating cellulose and chitin nanocrystals. J Membr Sci 544:261–271
43. Deitzel JM, Kleinmeyer J, Harris D, Tan NCB (2001) The effect of processing variables on the morphology of electrospun nanofibers and textiles. Polymer 42:261–272
44. Zhang Y, Zhang M, Cheng D, Xu S, Du C, Xie L, Zhao W (2022) Applications of electrospun scaffolds with enlarged pores in tissue engineering. Biomater Sci 10:1423–1447
45. Wang DK, Varanasi S, Fredericks PM, Hill DJT, Symons AL, Whittaker AK, Rasoul F (2013) FT-IR characterization and hydrolysis of PLA-PEG-PLA based copolyester hydrogels with short PLA segments and a cytocompatibility study. J Polym Sci Pol Chem 51:5163–5176
46. You ZR, Hu MH, Tuan-Mu HY, Hu JJ (2016) Fabrication of poly(glycerol sebacate) fibrous membranes by coaxial electrospinning: influence of shell and core solutions. J Mech Behav Biomed Mater 63:220–231
47. Fei PF, Liao L, Cheng BW, Song J (2017) Quantitative analysis of cellulose acetate with a high degree of substitution by FTIR and its application. Anal Methods 9:6194–6201
48. Kendouli S, Khalfallah O, Sobti N, Bensouissi A, Avci A, Eskizeybek V, Achour S (2014) Modification of cellulose acetate nanofibers with PVP/Ag addition. Mater Sci Semicond Process 28:13–19
49. Pereira AGB, Fajardo AR, Gerola AP, Rodrigues JHS, Nakamura CV, Muniz EC, Hsieh YL (2020) First report of electrospun cellulose acetate nanofibers mats with chitin and chitosan nanowhiskers: fabrication, characterization, and antibacterial activity. Carbohydr Polym 250:116954
50. Liu Y, Wei HH, Wang Z, Li Q, Tian N (2018) Simultaneous enhancement of strength and toughness of PLA induced by miscibility variation with PVA. Polymers 10:1178
51. Henkel J, Woodruff MA, Epari DR, Steck R, Glatt V, Dickinson IC, Choong PFM, Schuetz MA, Hutmacher DW (2013) Bone regeneration based on tissue engineering conceptions — a 21st century perspective. Bone Res 1:216–248
52. Conte AA, Sun KT, Hu X, Beachley VZ (2020) Effects of fiber density and strain rate on the mechanical properties of electrospun polycaprolactone nanofiber mats. Front Chem 8:610
53. Fukushima K, Tabuani D, Arena M, Gennari M, Camino G (2013) Effect of clay type and loading on thermal, mechanical properties and biodegradation of poly(lactic acid) nanocomposites. React Funct Polym 73:540–549
54. Kim JS, Lee DS (2000) Thermal properties of electrospun polyesters. Polym J 32:616–618
55. Zong XH, Kim K, Fang DF, Ran SF, Hsiao BS, Chu B (2002) Structure and process relationship of electrospun bioabsorbable nanofiber membranes. Polymer 43:4403–4412
56. Merkle V, Zeng L, Teng W, Slepian M, Wu X (2013) Gelatin shells strengthen polyvinyl alcohol core–shell nanofibers. Polymer 54:6003–6007
57. Ng K, Azari P, Nam HY, Xu F, Pingguan-Murphy B (2019) Electrospin-Coating of Paper: a natural extracellular matrix inspired design of Scaffold. Polymers 11:650
58. Nakamura H (2007) Morphology, function, and differentiation of bone cells. J Hard Tissue Biol 16:15–22
59. Ghag AK, Gough JE, Downes S (2014) The osteoblast and osteoclast responses to phosphonic acid containing poly(ε-caprolactone) electrospun scaffolds. Biomater Sci 2:233–241
60. Kuru L, Griffiths GS, Petrie A, Olsen I (1999) Alkaline phosphatase activity is up regulated in regenerating human periodontal cells. J Periodontal Res 34:123–127